International Journal for Research in Engineering Application & Management (IJREAM)
ISSN : 2454-9150 Vol-07, Issue-04, JULY 2021

Optimal Fuel Consumption using PI-ANN based RSC Control Strategy on Wind Driven DFIG, DG and Solar PV Array

D. Sireesha, B.Tech. Student, EEE Department, Kallam Haranadhareddy Institute of Technology, Guntur (DT), Andhra Pradesh, India, sireeshadumala2000@gmail.com

Dr. K. Hari Krishna, Professor, EEE Department, Kallam Haranadhareddy Institute of Technology, Guntur (DT), Andhra Pradesh, India, harikrishnaketha81@gmail.com

Abstract—This paper focuses on developing a novel algorithm which dynamically optimizes the controllers of doubly fed induction generator (DFIG) driven by a wind turbine (WT) to increase DFIG transient performance in all wind speed conditions. PI-ANN is proposed to optimize parameters of PI controllers of DFIG's rotor side (RSC) at different wind speeds in order to maximize the damping ratios of the system eigen values in small signal stability analysis. Based on the optimal values and the wind speed data set, an artificial neural network (ANN) is designed, trained, and it has the ability to quickly forecast the optimal values of parameters. Adaptive PI controllers (including ANN) are designed which dynamically change PI gain values according to different wind speeds. Simulation done via MATLAB software for a micro grid based DFIG, and, DG, including with PV battery system. The results show that the DFIG of ANN based adaptive PI control could significantly contribute in the transient performance improvement in a wide wind speed range. Bidirectional buck/boost DC-DC converter, battery energy storage, diesel generator, doubly fed induction generator (DFIG), power quality, solar photovoltaic array, Wind Turbine.

Keywords — Bidirectional buck/boost DC-DC converter, battery energy storage, diesel generator, doubly fed induction generator (DFIG), power quality, solar photovoltaic array, Wind Turbine.

I. INTRODUCTION

Diesel generators (DGs) are highly regarded for the decentralized power generation also as backup power within the urban housing society for the subsequent reasons.

- DGs are transportable and dispatch able.
- They are of lower capital cost.
- DGs maintenance is easier.
- They need higher conversion efficiency as compared to alternative sources of energy leading to low specific greenhouse gas emission.

For the above reasons, they are wide used for the facility distribution of islands, commercial and military ships etc [4]. However, DGs suffer from the higher running value at the side of noise and air pollution. The running cost depends on quantity of fuel consumption supported the facility generation. This cost is reduced by putting in renewable energy (RE) sources appreciate wind, solar and biomass and so forth Moreover, RE primarily based power sources are pollution free and ample in nature. Among RE sources, wind and solar are thought-about to be additional common attributable to their reduced cost and technological advancements [5], [6]. Wind turbines are in the main classified as fastened speed and variable speed type. Fastened speed wind turbines are used earlier due to their easy in operation features. However, they suffer with additional power loss. Variable speed wind turbines with doubly fed induction generator (DFIG), are dominantly used for wind energy extraction because of its advantages such as reduced device rating, less acoustic noise, extremely energy economical and low power loss [7]. Substantial literature on DFIG primarily based wind energy conversion system (WECS) each in standalone [8] and grid connected modes, is out there [9]-[11]. In [8], the authors have bestowed DFIG based WECS operating in standalone with electric battery energy storage (BES) connected directly at the DC link. Moreover, the comparative performance with and without BES is mentioned. In [9], the authors have represented associate degree extended active power theory for effective operation of turbine coupled DFIG each in balanced and unbalanced grid conditions. Moreover, the DFIG is management led with solely rotor facet device (RSC). Therefore, the topology suffers from the facility quality problems particularly throughout harmonic loads. Liu et al. [10] have investigated the influence of section barred loop parameters and grid strength on the soundness

 DOI : 10.35291/2454-9150.2021.0380

of DFIG wind energy facility in grid connected mode. However, an experimental validation has not been performed. In [11], the authors have discussed a synchronization control methodology for smooth association of DFIG to the grid. Moreover, it's been enforced on a changed IEEE thirty-nine bus system victimization real time simulation platform. However, hardware realization has not been done. In alternative side, there has been increasing power generation through solar photovoltaic (PV) array worldwide. The solar energy conversion system (SECS) may be single stage or double stage. a number of the literature relating to solar PV system is reported in [12], [13]. Shah of Iran et al. [12] has incontestable the one stage SECS connected to the utility grid. Moreover, a basic current extraction technique supported second-order generalized planimeter with frequency-locked loop has been enforced for voltage source conversion (VSC). In [13], the authors have bestowed the double stage SECS interacting to the grid. In addition, associate degree adjustive algorithmic rule of quick zero attracting normalized least mean fourth has been implemented for VSC to boost the facility quality issues. The operation of WECS and SECS separately, isn't economical and reliable attributable to their intermittency. Therefore, the mixing of each wind and solar sources, improves reliability of power generation [14], [15]. Morshed et al. [14] have presented wind-PV system with fault ride through capabilities. In its topology, the solar PV array is connected at the DC link of DFIG primarily based WECS through a boost converter and a DC-DC converter. However, it will increase the shift losses and cost, because of additional DC-DC converter along with grid side converter. In [15], the authors have incontestable the wind-solar PV system with BES in standalone mode. In its configuration, the solar PV array is connected at the DC link of wind turbine driven DFIG through a boost converter. However, the present through BES isn't controlled, as a result of its directly connected at the DC link. Further, the micro grids supported dg, wind and solar sources are developed and reportable within the literature [16]-[18]. In [16], the authors have mentioned the capability coming up with of BES for a micro grid based on wind, solar and diesel sources that are placed in island. However, optimum fuel operation of DG has not been discussed. In [17], the authors have incontestable a wind-diesel micro grid for fuel economical zone with BES. However, the BES current is not controlled because of its direct association at the DC link. Moreover, the possibilities of obtaining aloof from fuel economical zone are a lot of because of association of only 1 RE supply. However, the optimum operation of metric weight unit has been neglected whereas developing the source and cargo controllers. In any micro grid, the BES plays vital role during the pair of generation and demand. Moreover, it helps in extraction of most power each from wind and solar, particularly when the generation is over the demand. There are several maximum power point tracking (MPPT) techniques discussed within the literature, each for wind and solar to extract most power adore particular wind speed and isolation, severally. This work presents a micro grid supported wind turbine driven DFIG, dg and solar PV array with BES, so as to reduce the fuel consumption of dg. In this, the DG is designed to deliver the bottom load demand of a specific social unit locality. The most contributions of this study are on the management aspects of the scheme that are as follows.

- A completely unique generalized thought is used to compute the reference dg power output for the dg to stay operative in optimum fuel consumption mode.
- The load side device control (LSC) is meant to regulate dg beside the power quality problems admire load unbalance compensation, harmonics compensation and reactive power compensation.
- The RSC control is designed to extract most power from the wind turbine.
- The BES is connected to the common DC bus of back-back connected VSCs through a bifacial buck/boost DC-DC converter. It aims to supply path for excess mechanical device power of DFIG. Moreover, a solar PV array is directly connected at DC bus.
- The bidirectional buck/boost DC-DC converter control is meant in very thanks to extract most power from the solar PV array and to regulate the present through BES.
- A changed perturb and observe (P&O) MPPT algorithm is presented to get maximum power from a solar PV array.
- This micro grid configuration is enforced with minimum variety of converters, thereby reducing the full system value and switching losses.
- The DFIG stator currents and dg currents are maintained balanced and sinusoidal, as per the IEEE 519 standard.

The wind-diesel-solar micro grid with BES is modelled and simulated using Sim Power Systems tool box of MATLAB. The system performance is analyzed for variable wind speeds, variable insolation, impact on buck boost device at varied masses and unbalanced nonlinear load connected at purpose of common coupling (PCC). To validate the micro grid operation, tests are performed on a developed prototype within the laboratory.

II. CONFIGURATION OF MICROGRID

The schematic configuration of the micro grid is depicted in Figure. It consists of wind turbine, DFIG, DG, solar PV array, BES, bidirectional buck/boost DC-DC converter, RSC, LSC, interfacing inductors, Δ/Y transformer, linear and nonlinear loads, circuit breakers (CB_1 & CB_2), DC link capacitor and ripple filters etc. This micro grid is designed to deliver a peak load of 7.5 kW for a particular locality. The wind turbine generator and solar PV array are designed

 DOI : 10.35291/2454-9150.2021.0380

to deliver a power of 7.5 kW each. In this scheme, the solar PV array is directly connected to DC link, whereas BES is connected through bidirectional buck/boost DC-DC converter. The DG comprises of a synchronous generator of 4 pole, internal combustion engine of 4 stroke reciprocating type along with automatic voltage regulator (AVR). A 7.5 KVA DG is selected in line with rated capacity of the wind turbine generator. The design of a wind turbine generator, solar PV array, DG, BES and other components, is carried out based on the literature reported in [12], [15], [17]. Moreover, the design parameters of micro grid are given in Appendices.

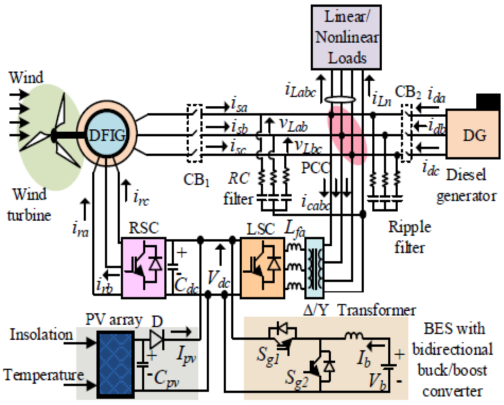

Fig.1. DFIG based micro grid.

A. Control Algorithm for RSC

The control algorithm of RSC is depicted in Fig. 2. The RSC is used to supply the reactive power requirement of DFIG

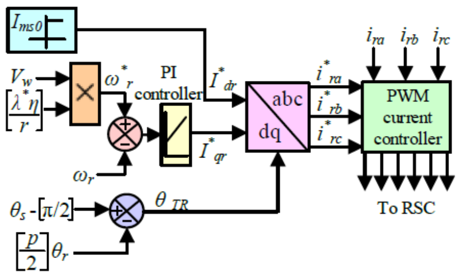

Fig.2. RSC control algorithm

To regulate the speed for achieving MPPT from the wind turbine, the field-oriented vector control (FOVC) is used for RSC to generate the switching pulses, as shown in Fig. 2. In FOVC, direct axis and quadrature axis components of rotor currents (I^*_{dr}, I^*_{qr}) represent reactive and active components, respectively. The I^*_{dris} corresponding to no load magnetizing current (I_{ms0}) of DFIG, which is computed as [21],

$$I_{ms0} = \frac{\sqrt{2}V_L}{\sqrt{3}X_m} \quad (1)$$

Where X_m denotes the magnetizing reactance of the machine and V_L is the line voltage at the machine terminals.

The I^*_{qris} estimated by passing the speed error through proportional and integral (PI) controller as depicted in Fig. 2 and it is derived as,

$$I^*_{qr(k)} = I^*_{qr(k-1)} + K_{p\omega}(\omega_{err(k)} - \omega_{err(k-1)}) + K_{i\omega}\omega_{err(k)} \quad (2)$$

Where $K_{p\omega}$ and $K_{i\omega}$ represent proportional and integral constants of PI speed controller, respectively. The $\omega_{err}(k)$ and $\omega_{err}(k-1)$ denote speed error at k^{th} and $(k-1)^{th}$ instants, respectively.

The $\omega_{err}(k)$, is obtained as,

$$\omega_{err(k)} = \omega^*_{r(k)} - \omega_{r(k)} \quad (3)$$

Where $\omega^*_r(k)$ and $\omega_r(k)$ denote the reference and sensed rotor speed of DFIG at k^{th} instant, respectively.

The reference rotor speed is obtained from the tip speed ratio MPPT control [19] as,

$$\omega^*_r = \eta\lambda^* V_w / r \quad (4)$$

Where V_w λ^*, η, and r represent wind speed, optimal tip speed ratio, gear ratio and radius of wind turbine, respectively.

The rotor transformation angle (θ_{TR}) is computed as,

$$\theta_{TR} = \left(\theta_s - \frac{\pi}{2}\right) - \left(\frac{p}{2}\right)\theta_r \quad (5)$$

Where θ_s is obtained from phase locked loop and θ_r is computed from the sensed rotor speed as,

$$\theta_r = \int_0^t (\omega_r)dt \quad (6)$$

Finally, reference rotor currents (i^*_{ra}, i^*_{rb} and i^*_{rc}) are derived from I^*_{qr} and I^*_{dr} using an angle of transformation θ_{TR}, as depicted in Fig.2. These reference currents along with sensed rotor currents (i_{ra}, i_{rb} and i_{rc}), are applied to pulse width modulation (PWM) controller to produce RSC gating signals.

B. Control Algorithm for LSC

The LSC control algorithm is depicted in Fig. 3. The LSC is controlled to achieve the following objectives.

DOI : 10.35291/2454-9150.2021.0380

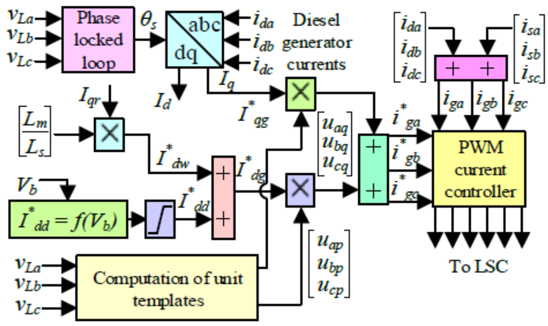

Fig.3. LSC control algorithm

It maintains the DG and DFIG stator currents sinusoidal and balanced. It regulates the DG power within the range of P_{Dmin} to P_{Dmax} to achieve optimal fuel consumption. Where P_{Dmin} and P_{Dmax} refer to minimum and maximum DG power output in pu for optimal fuel consumption.

A modified indirect vector control based on voltage-oriented reference frame is used to generate the reference currents as shown in Fig. 3. In this, both DG and DFIG stator currents are added and controlled to extract maximum power from the DFIG and to regulate the DG power within the range for optimal fuel consumption. The d-axis component of LSC is obtained as,

$$I^*_{dg} = I^*_{dd} + I^*_{dw} \quad (7)$$

Where I^*_{dd}, I^*_{dw} denote the d-component current of DG and DFIG, respectively. It is noted that the saturation block is placed before the I^*_{dd} component to operate the DG in optimal fuel efficient zone at change in load, as depicted in Fig. 3.

In this work, a generalized concept is used to calculate the DG power based on state of the BES. The reference DG power in pu (P*D) is computed as,

$$P^*_D = P_{D\min} + k_1\beta \quad (8)$$

Here the value of β varies from 0 to 1. The minimum value of β is achieved when BES is charged to maximum voltage ($V_{b\,max}$) whereas β takes maximum value when BES voltage falls to its minimum value ($V_{b\,min}$). The β is of the form as,

$$\beta = \frac{V_{b\max} - V_b}{k_2} \quad (9)$$

In (8) and (9), k_1 and k_2 represent constant parameters. The value of k_1 is selected such that P*D attains its maximum limit of optimal fuel consumption as β tends to unity. Moreover, the value of k_2 is selected such that the β attains unity at V_{bmin}. In this work, the chosen values of P_{Dmin}, P_{Dmax}, V_{bmax}, V_{bmin}, k_1 and k_2 are mentioned in Appendices.

From (8), the I^*_{dd} is computed as,

$$I^*_{dd} = \left(\sqrt{2/3}\right) \times \left(\frac{P^*_D \times VA_{DG}}{V_L}\right) \quad (10)$$

Where V_L and V_{ADG} represent line voltage at PCC and VA rating of DG, which is chosen as a base value.

The I_{dw}*is computed as,

$$I^*_{dw} = \left(\frac{L_m}{L_s}\right) I_{qr} \quad (11)$$

The DG currents (i_{da}, i_{db} and i_{dc}) are transformed to Id and I_q using angle of transformation (θ_s), which is obtained from PLL as shown in Fig. 3. The q-axis component of LSC current (I_{qg}*) is numerically same as I_q of DG. The I_{dg}*and I_{qg}*are multiplied with in-phase and quadrature unit templates, respectively and then added together to generate current references (i_{ga}*, i_{gb}*and i_{gc}*). The unit templates are obtained from phase voltages (v_a, v_b and v_c), as shown in Fig. 3. Unit templates of in-phase components are obtained as,

$$u_{ap} = \frac{v_a}{V_m}, u_{bp} = \frac{v_b}{V_m}, u_{cp} = \frac{v_c}{V_m} \quad (12)$$

Where, V_m denotes the peak of phase voltage at PCC, which is computed as,

$$V_m = \{2(v_a^2 + v_b^2 + v_c^2)/3\}^{1/2} \quad (13)$$

The unit templates of quadrature components, are obtained from in-phase components as,

$$\left.\begin{aligned} u_{aq} &= -\frac{u_{bp}}{\sqrt{3}} + \frac{u_{cp}}{\sqrt{3}}, u_{bq} = \frac{\sqrt{3}u_{ap}}{2} + \frac{u_{bp} - u_{cp}}{2\sqrt{3}}, \\ u_{cq} &= -\frac{\sqrt{3}u_{ap}}{2} + \frac{u_{bp} - u_{cp}}{2\sqrt{3}} \end{aligned}\right\} \quad (14)$$

Finally, the generated reference currents and sensed currents (i_{ga}, i_{gb} and i_{gc}) are applied to PWM controller to produce pulses for LSC, as depicted in Fig. 3.

C. Solar PV Array MPPT Algorithm and Bidirectional Buck/Boost DC-DC Converter Control

The bidirectional buck or bidirectional boost DC-DC converter is used to regulate the DC link voltage by controlling power flow through the BES. By doing so, the solar MPPT is achieved. In this, a modified perturb and observe (P&O) algorithm is used, which consists of sampling pulse generation (X) and subsequently estimation of reference DC link voltage (V^*_{dc}) as depicted in Figs. 4-5, respectively. Fig. 4 illustrates various steps involved in the generation of sampling pulse 'X'. Here, the sampling pulse

 DOI : 10.35291/2454-9150.2021.0380

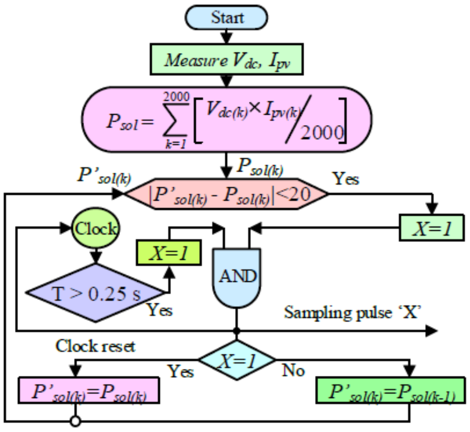

Fig. 4 Sampling pulse generation

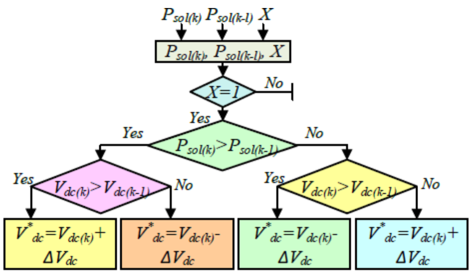

Fig.5. MPPT algorithm of solar PV array

is a name given to variable 'X'. It varies between digital bits 0 and 1. In Fig. 4, the first step is to get the information of DC link voltage or solar PV voltage (V_{dc}) and solar PV current (I_{pv}) at k^{th} instant and computation of instantaneous solar power. The second step is the determination of running average solar power (P_{sol}), which performs the same function as filtering. In case the absolute difference between the running averaged power (P_{sol}) and previously sampled power (P_{sol}) is less than 20 W combined with minimum time delay of 0.25 s from previous sampling, the control senses that steady state has arrived. On sensing the steady state, the output of the sampling pulse 'X' becomes '1'. The sampling pulse decides the instant of incremental change in reference DC link voltage (V^*_{dc}) or solar PV MPPT voltage. The value of V^*_{dc} is updated only if sampling pulse becomes '1'. This is clearly evident from Fig. 5 that depicts the modified P&O MPPT algorithm. Once X becomes '1', the MPPT algorithm checks for $P_{sol}(k) > P_{sol}(k\text{-}1)$. If it is yes, then it again checks for $V_{dc}(k) > V_{dc}(k\text{-}1)$. If it is also yes, then, the new reference DC link voltage becomes $V^*_{dc} = V_{dc}(k) + \Delta V_{dc}$. Where ΔV_{dc} denotes the small incremental change in DC link voltage. The other scenarios are evident from the Fig. 5.

The bidirectional buck/boost DC-DC converter control is demonstrated in Fig. 6. The outer proportional-integral (PI) controller of the bidirectional buck or bidirectional DC-DC boost converter control, is used to regulate the DC link voltage. Moreover, the output of the outer PI controller is reference battery current (I^*_b), as depicted in Fig. 6. The inner PI controller is used to track the reference battery current. Moreover, the output of the inner PI controller is the duty ratio (R) of the bidirectional buck/boost DC-DC converter. From Fig. 6, the reference battery current (I^*_b) is obtained as,

$$I^*_{b(k)} = I^*_{b(k-1)} + K_{pb}(V_{de(k)} - V_{de(k-1)}) + K_{ib} V_{de(k)} \quad (15)$$

Where, error of the DC link voltage at k^{th} instant is $V_{de(k)} = V^*_{dc(k)} - V_{dc(k)}$. Here $V^*_{dc}(k)$ and $V_{dc}(k)$ represent the reference DC link voltage and sensed DC link voltage at k^{th} instant, respectively. K_{pb} and K_{ib} denote the proportional and integral constants of the outer PI controller.

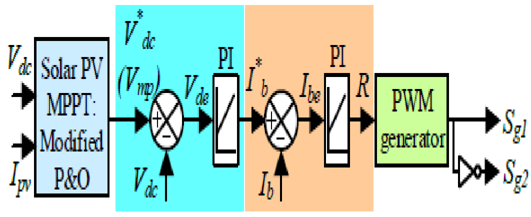

Fig. 6. Control of bidirectional buck or bidirectional boost converter.

Besides, the duty ratio (R) of the bidirectional DC-DC converter, is computed as,

$$R_{(k)} = R_{(k-1)} + K_{pr}(I_{be(k)} - I_{be(k-1)}) + K_{ir} I_{be(k)} \quad (16)$$

Where, error of the battery current at k^{th} instant is $I_{be(k)} = I^*_{b(k)} - I_{b(k)}$. Here $I^*_b(k)$ and $I_b(k)$ represent the reference battery current and sensed battery current at k^{th} instant, respectively. The obtained duty ratio (R) is applied to PWM generator to produce pulses for the switches of the bidirectional buck or bidirectional boost converter.

III. DEVELOPING CONTROL FOR THE NEW SCHEME

The TSG system consists of a tidal stream turbine (TST) coupled to a Doubly Fed Induction Generator (DFIG) connected to the grid through the back-to-back power device as shown in. The turbine converts the K.E. from the current speed to the rotation of the rotor head. The DFIG is coupled to the rotor shaft through the drive-train, which is customized to the grid through the back-to-back power converters. The management strategy describes however the tidal turbine is intended to approach the steady state of the ideal power curve. This amounts to adjusting the values of power and rotor speed at steady-state for every recurrent event speed within the vary of the rotary engine operation. The system could vary from one region of operation to another. The ANN block provides two reference trajectories to the system: the acceptable movement speed reference following the MPPT strategy to maximize the extracted power; and therefore, the adequate angle of attack of the

 DOI : 10.35291/2454-9150.2021.0380

turbine blades to limit the power captured in the case of high tidal current speed. The management of the electrical a part of the system is dedicated to the DFIG specializing in the active and reactive powers' control. This control approach is realized by the ability physics converters similar to the Rotor side converter (RSC) and therefore the Grid side converter (GSC). The RSC aims to maintain the movement speed of the generator at AN optimum price and

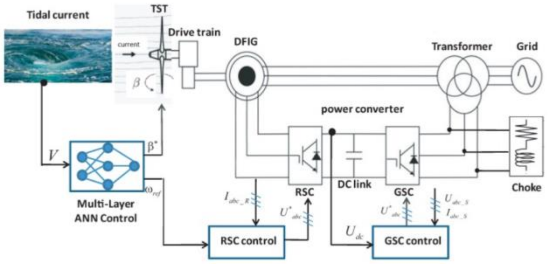

Fig.7. DFIG based microgrid with PI-ANN

minimizes the core losses while the GSC is employed to maintain the voltage of the DC-link and controls the output reactive power.

IV. The Newly Proposed RSC-Based Scheme with the PI-ANN Hybrid Controller and SCC

The reference voltage values V_{dqr}* for the RSC are computed from the outputs of two PI-ANN controllers as described in Fig. 8. The PI-ANN controllers can enhance remarkably the independence with parametric alterations of the power system in generating the reference signals. Also, using the PI with anti-windup (PI+A) controllers, values of I_{dqr}* can be obtained suitably from errors between the reference and measured signals of the two powers. As aforementioned, the Notch filters are utilized to reject the negative sequence components. Nonetheless, the real response and efficacy of digital Notch filters are not entirely flawless; thus, the SCC, containing the two PI controllers, is designed for combining with the Notch filters to can remove thoroughly the negative sequence components of rotor current. In SFOC, with I_{dqr}= 0, ψ_{qr} = 0 and, the rotor current now can be defined by Besides, the output values of the SCC are I_{dqr}*, so it also has function as a current sub-controller for the PI-F and PI–ANN controllers to help regulate the positive sequence components of rotor current. Meanwhile, note that negative sequence components of the rotor current will boost the power rating of RSC if they are utilized in stabilizing the two output powers of DFIG. From, the output active power P_s and reactive power Q_s in stator are computed as follows:

Structure of the PI-ANN hybrid controller is shown in fig (8).

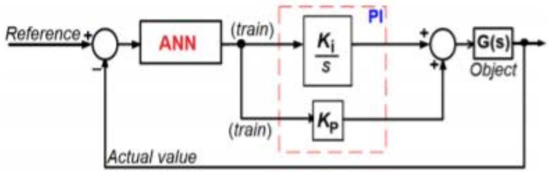

Fig. 8 Design diagram of the PI-ANN controller

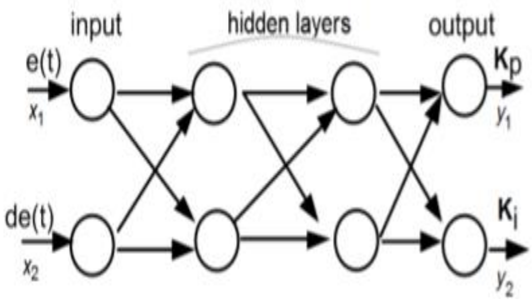

Fig. 9 Detailed structure of the ANN with four layers

The proposed ANN in this study utilizing RSC control algorithm for performing an offline training process to determine suitable values for the key two coefficients K_P and K_I of the PI controller. As given in Fig. 8, the ANN comprises one input layer, two hidden layers and one output layer. Wherein, the input layer has two neurons as the error value e(t) and its derivative value de(t) of the current as shown in Fig. 9, each hidden layer has two neurons, and the output layer has two neurons as K_P and K_I. The total weight value net_q and the output value Z_q of the j^{th} neuron in the q^{th} hidden layer are computed, respectively

$$net_q = \sum v_{qj} x_j \quad (17)$$

$$Z_q = a_h(net_q) = a_h(\sum v_{qj} x_j) \quad (18)$$

Where v_{qj} is the weight gain for the j^{th} neuron, and is the operational function used for the q^{th} hidden layer. Then, the total weight value of the i^{th} neuron in the output layer is expressed, where w_{iq} is the weight gain for the i^{th} neuron. Lastly, the two coefficients K_P and K_I are defined by respectively; where a_0 is the operational function used for the output layer.

$$net_i = \sum w_{iq} Z_q = \sum [w_{iq}.a_h(net_q)] \quad (19)$$

$$K_P = a_0(net_1) = a_0(\sum w_{1q} Z_q) = a_0(\sum [w_{1q}.a_h(net_q)]) \quad (20)$$

$$K_I = a_0(net_2) = a_0(\sum w_{2q} Z_q) = a_0(\sum [w_{2q}.a_h(net_q)]) \quad (21)$$

Where operational functions in hidden and output layers are bipolar sigmoid and linear functions, respectively:

$$a_h(f) = 1/(1 + e^{-f}) \quad (22)$$

$$a_0(f) = f \quad (23)$$

 DOI : 10.35291/2454-9150.2021.0380

If the number of hidden layers is increased, ANN may have a better adaptation. In this study, to evaluate the proposed PI-ANN algorithm, two hidden layers can be used such as the simplest structure for implementing in simulation. Where the number of hidden layers is more, the training time becomes longer; which can lead to cause noticeable delay in generating the control signal at output layer. So optimization for the number of hidden layers and time delay will be studied in our future work. As shown in Figs. 8 and 9, the BP algorithm has two main steps in transmitting information between layers as follows. Firstly, the input data x(k) is transmitted forward to generate the value y(k) at the output. Then, the error value E(k) between the reference value in the data set d(k) and the above output value y(k) is transmitted back to the previous layer to update fittingly the weight gains v_{qj}. The data set utilized for the offline training process is S{x(k),d(k)}, and the goal of this training process is to minimize the error E(k+1) as given. Normally, the offline training process in ANN is performed sometimes with several data sets to achieve a good result as desired.

$$E(k+1) = E(k) + 0.5\sum[d_i(k) - y_i(k)] \rightarrow \min \quad (24)$$

V. Simulation Results for the New DFIG Scheme

The microgrid based on wind turbine driven DFIG, DG and solar PV array with BES, is simulated using MATLAB. Various signals used to analyze the system performance, are rms value of phase voltage (V_r), system frequency (f_L), DFIG rotor speed (ω_r), DG power (P_D), wind power from stator (P_w), solar PV power (P_{sol}), load power (P_L), LSC power (P_{LSC}), DC link voltage (V_{dc}), battery current (I_b), battery voltage (V_b), wind speed (V_w), insolation (G), rotor power coefficient (C_p), a-phase stator current (i_{sa}), rotor currents (i_{rabc}), a-phase DG current (i_{da}), a-phase PCC voltage (v_{La}), stator currents (i_{sabc}), DG currents (i_{dabc}), load currents (i_{La}, i_{Lb} and i_{Lc}), neutral current (i_{Ln}) and LSC currents (i_{cabc}). The parameters used for the simulation are mentioned in Appendices.

A. Performance of Bidirectional Buck/Boost DC-DC Converter at Change in Load

The performance of bidirectional buck or bidirectional boost DC-DC converter at change in the load is depicted in Figs.10. The wind speed and insolation are kept at 7 m/s and 700 W/m2, respectively. Initially a 3-phase balanced load of 2.5 kW is connected at PCC. The DG is delivering 4.84 kW (shown in Fig.10), which corresponds to the battery bank voltage of 125 V. Moreover, the DFIG and solar PV array powers are 2.013 kW and 4.122 kW, respectively as depicted in Fig.10. Since the total generation is more than the local demand, the remaining power goes to BES through a bidirectional buck/boost DC-DC converter as shown in Fig. 10. At t = 3 s, an additional load of 2 kW is connected and again it is disconnected at t = 5.5 s. During this period, it is observed that the power generation from all sources, remains unchanged and the increased load power is met by the BES through LSC. There is minor sag and swell of DC link voltage, however, the solar MPPT is unaffected as seen from P_{sol} waveform. Moreover, the system voltage and frequency are maintained constant, as depicted in Fig.10.

B. System Performance at Variable Wind Speeds

The performance of the system at variable wind speeds are depicted in Figs. 11. In this, a 3-phase load of 4 kW is connected at PCC and the insolation is kept at 700 W/m^2. The DG delivers power of 5.67 kW based on the state of the BES, as depicted in Fig. 11. The pattern of wind speed variation is depicted in Fig.11. It is observed that the controller regulates the DFIG rotor speed as per wind MPPT algorithm, as depicted in Fig. 11. Moreover, it is observed that the DC link voltage is regulated. The system dynamic response during the transition of DFIG speed from super synchronous to sub synchronous speed region is depicted in Fig.11. It is observed that wind MPPT is obtained during the variation of wind speed. Moreover, the frequency rotor currents, is changed according to the speed of operation of DFIG.

C. System Performance at Variable Insolation

The performance of the system at varying solar radiation is depicted in Fig.12. In this, the wind speed is kept constant at 7 m/s. Moreover, the DG delivers 4.2 kW power based on the battery voltage, as depicted in Fig.12. In this, a 3-phase linear balanced load of nearly 4 kW is connected at PCC. The insolation of solar PV array is varied from 700 W/m^2 to 800 W/m^2 at t = 3 s and again it is reduced to 600 W/m^2 at t = 5.5 s, as depicted in Fig.12. The DC link voltage is regulated by the bidirectional DC-DC converter control for achieving the solar MPPT. Moreover, the solar MPPT is manifested by the P_{sol} waveform, as depicted in Fig.12.

D. System Performance at Unbalanced Nonlinear Load

The dynamic performance of the system at unbalanced nonlinear load is depicted in Fig. 13. Initially, a balanced load of 6.7 kW is connected at PCC. It includes a linear load of 0.5 kW and remaining be the nonlinear load, connected on each phase. At t = 2.6 s, a-phase of the load is disconnected and subsequently phase-b, is also disconnected at t = 2.8 s, as depicted in Fig. 10. However, both voltages and currents of DFIG and DG are maintained balanced and follow the IEEE 519 standard. The LSC helps in unbalance and harmonics compensation of the connected load at PCC. The LSC currents and neutral current are also shown in Fig. 13. Moreover, the variation of power at unbalanced nonlinear load is depicted in Fig. 13. Fig. 13 demonstrates waveforms of V_r, V_{dc}, I_b, P_{sol}, P_w, P_D, P_L and P_{LSC}. From these results, it is observed that the DC link voltage is regulated and moreover, solar PV and wind

 DOI : 10.35291/2454-9150.2021.0380

MPPT operation is unaffected. The decrease in load power goes to BES through LSC, which is evident from I_b, P_L and PLSC waveforms. Moreover, V_r is maintained at constant value.

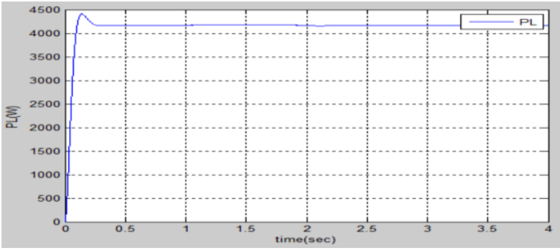

(a)

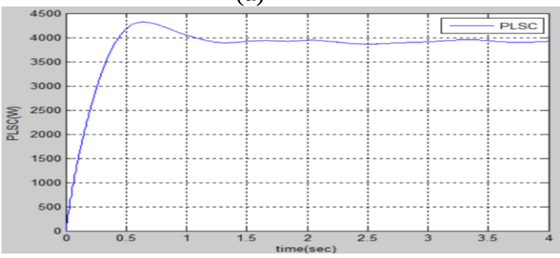

(b)

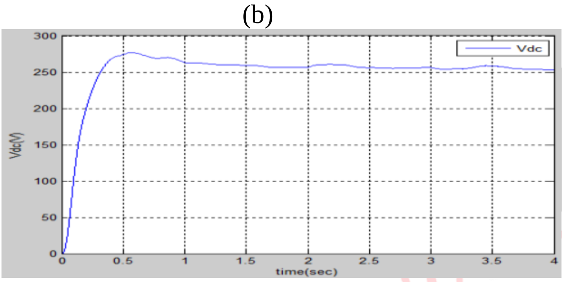

(c)

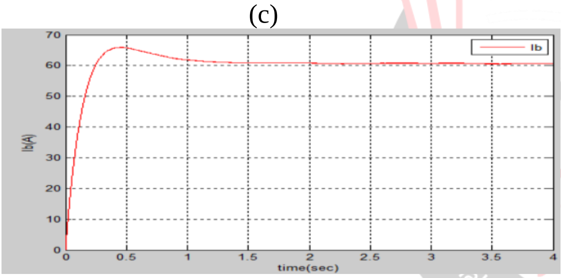

(d)

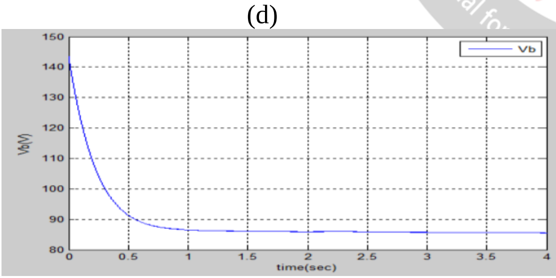

(e)

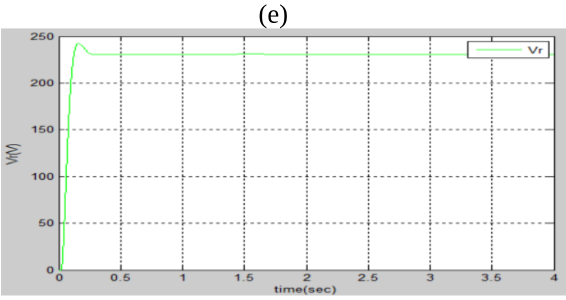

(f)

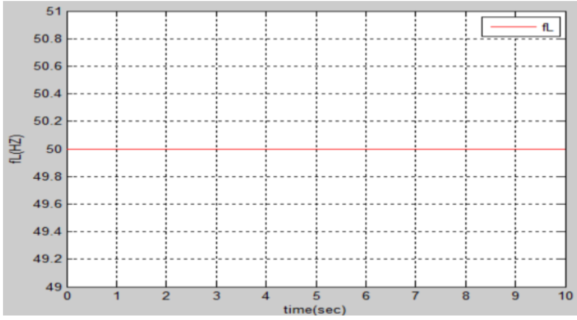

(g)

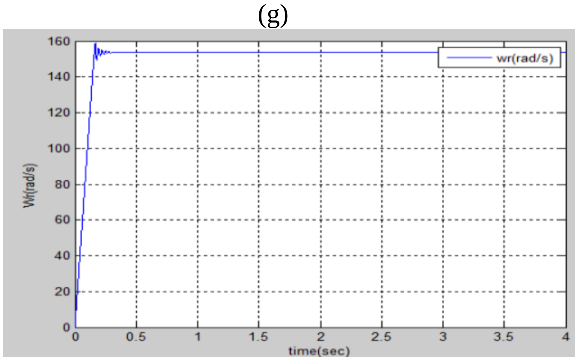

(h)

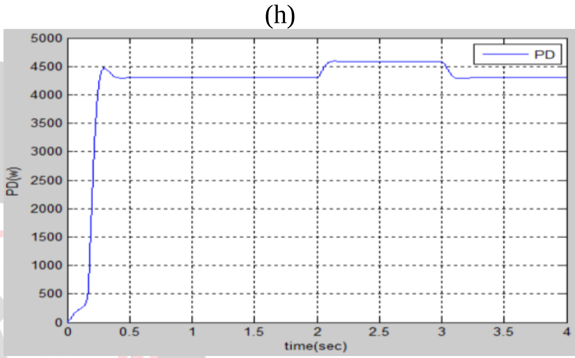

(i)

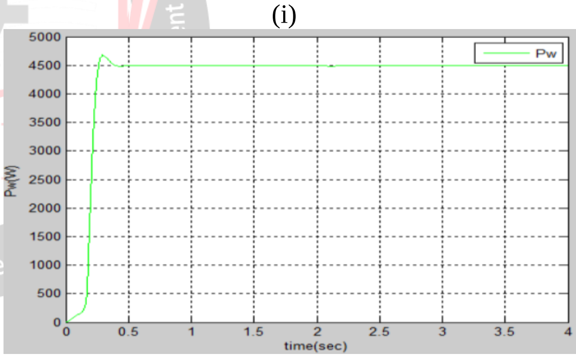

(j)

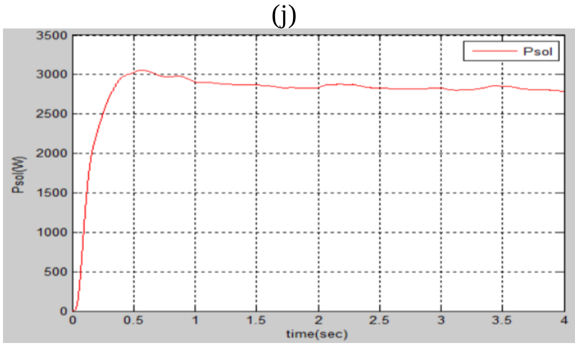

(k)

Fig. 10. (a-b) Performance of bidirectional buck/boost converter at change in load (a) P_L, P_{LSC}, V_{dc}, I_b and V_b(b) V_r, f_L, ω_r, P_D, P_w and P_{sol}.

 DOI : 10.35291/2454-9150.2021.0380

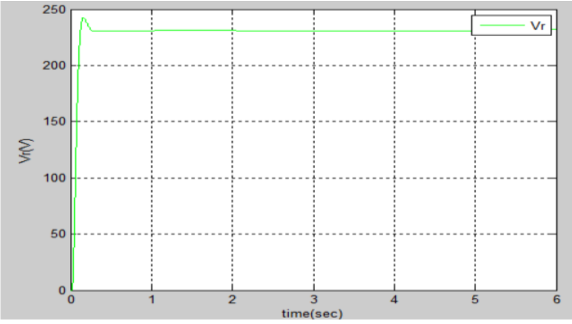

(a)

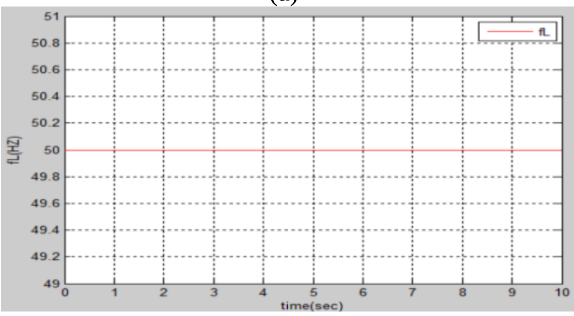

(b)

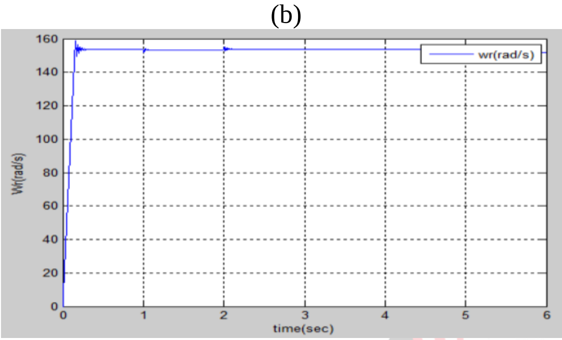

(c)

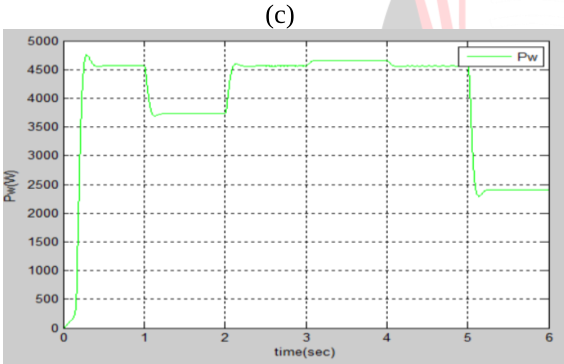

(d)

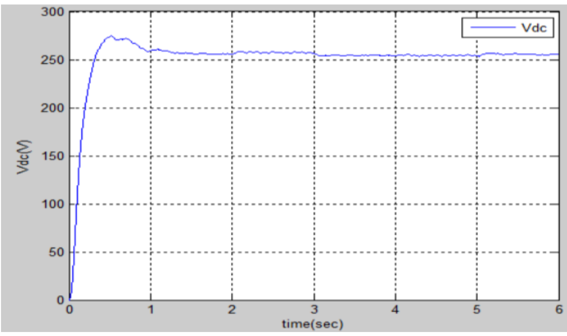

(e)

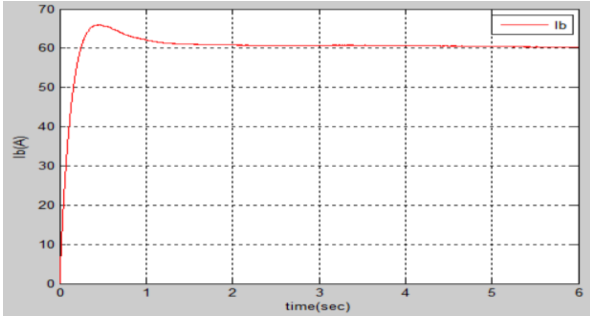

(f)

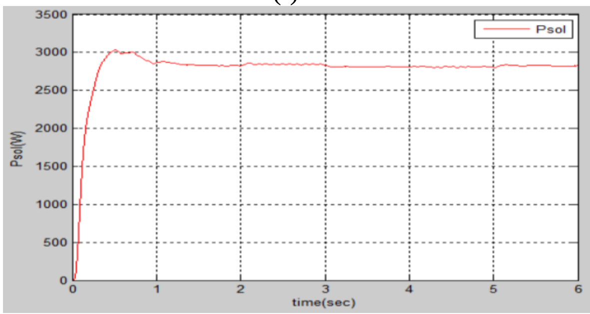

(g)

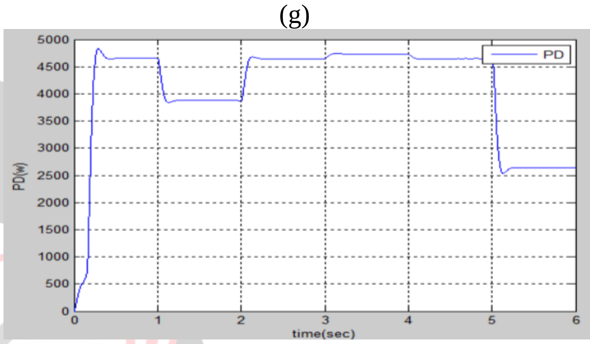

(h)

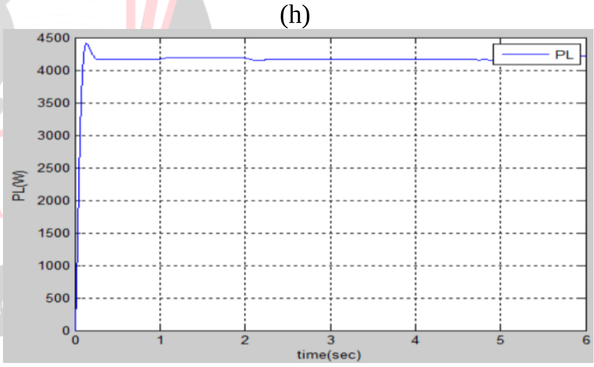

(i)

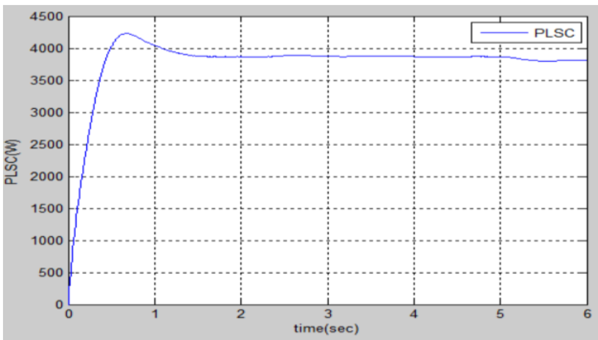

(j)

 DOI : 10.35291/2454-9150.2021.0380

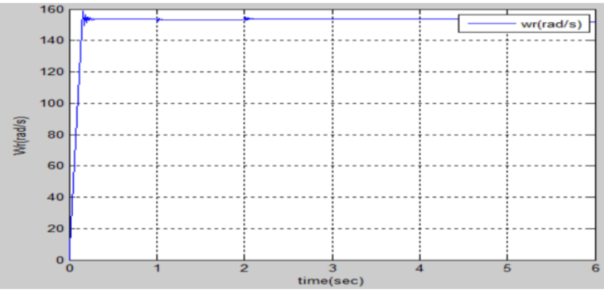

(k)

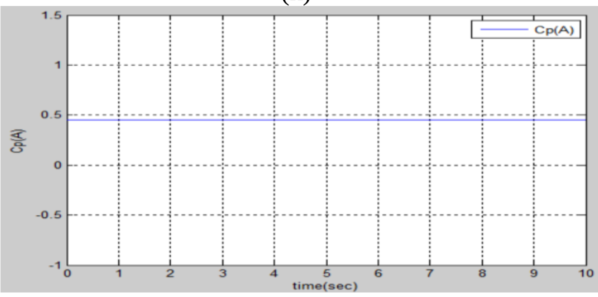

(l)

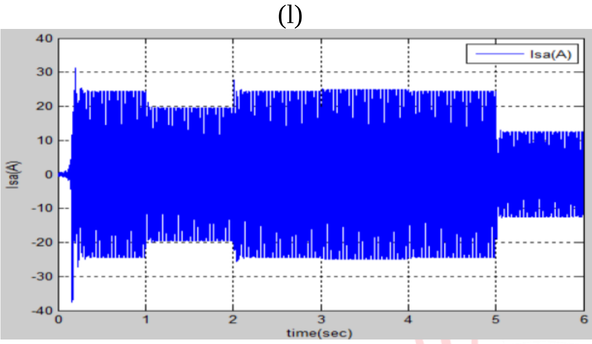

(m)

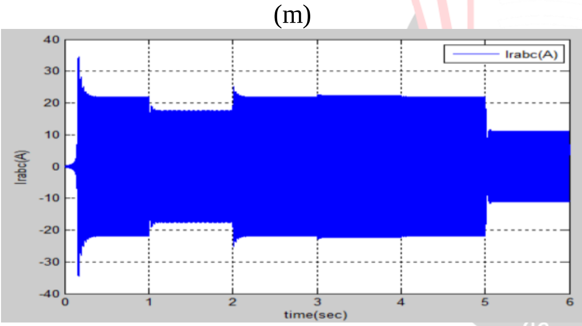

(n)

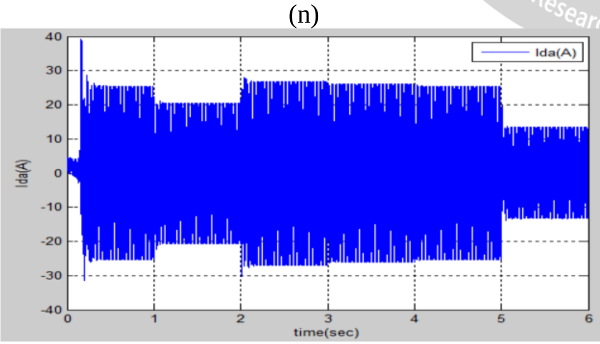

(o)

Fig. 11. System performance at variable wind speed (a) V_r, f_L, V_w, ω_r and P_w (b) V_{dc}, I_b, P_{sol}, P_D, P_L and P_{LSC}. (c) System performance during changeover of DFIG speed from super synchronous to sub synchronous speed region: V_w, ω_r, C_p, i_{sa}, i_{rabc} and i_{da}.

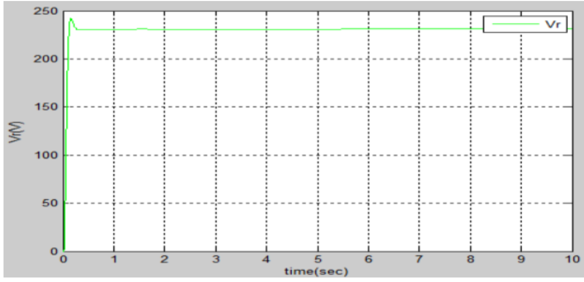

(a)

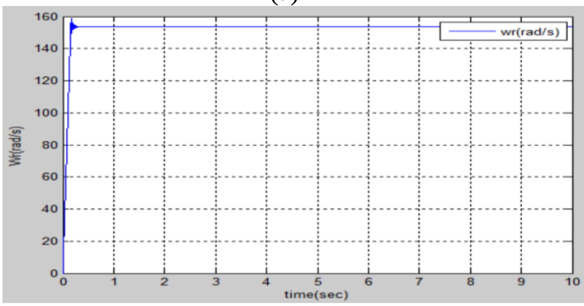

(b)

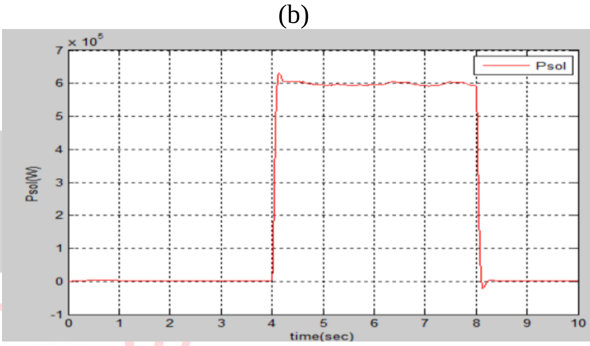

(c)

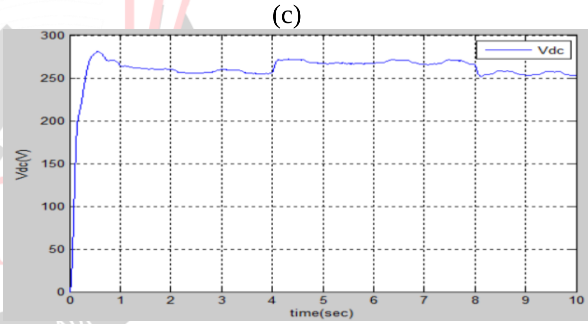

(d)

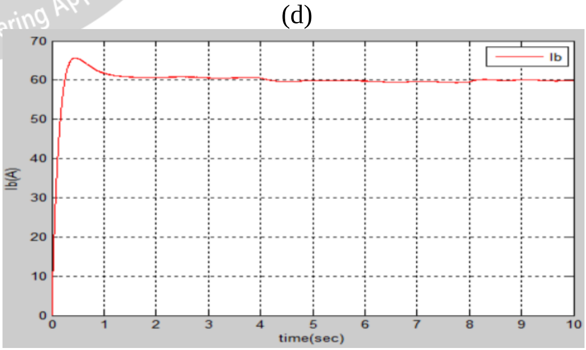

(e)

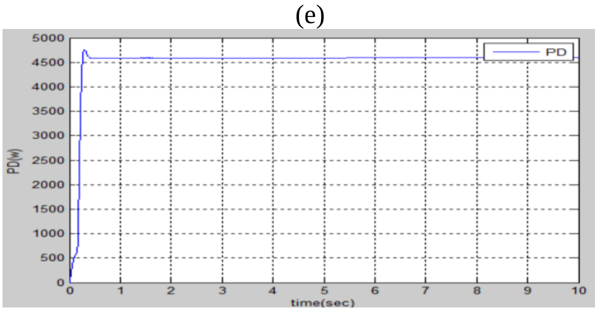

(f)

 DOI : 10.35291/2454-9150.2021.0380

International Journal for Research in Engineering Application & Management (IJREAM)
ISSN : 2454-9150 Vol-07, Issue-04, JULY 2021

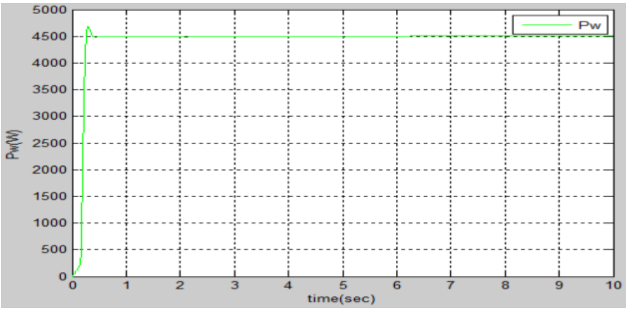

(g)

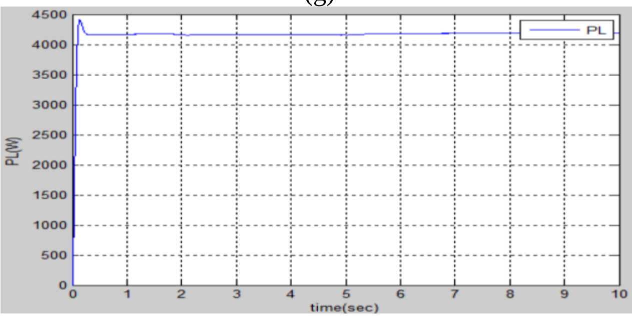

(h)

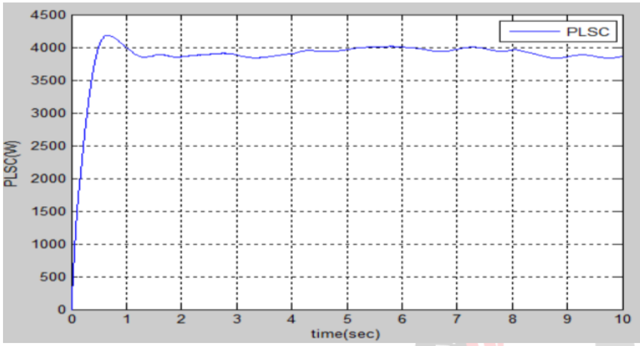

(i)

Fig.12. System performance at variable insolation(a)V_r, ω_r, P_{sol} and V_{dc} (b) I_b, P_D, P_w, P_L and P_{LSC}.

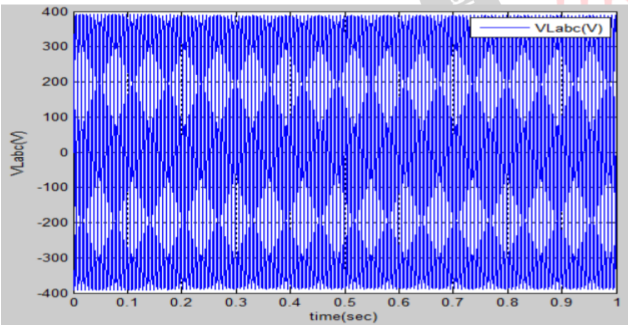

(a)

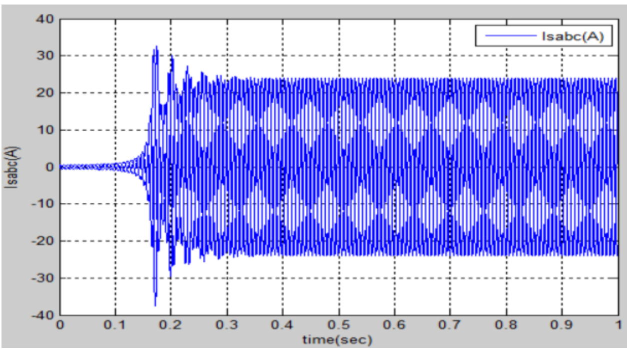

(b)

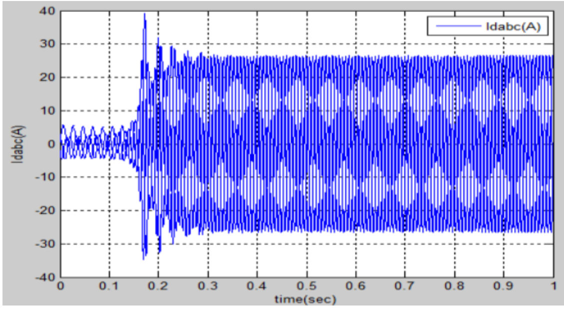

(c)

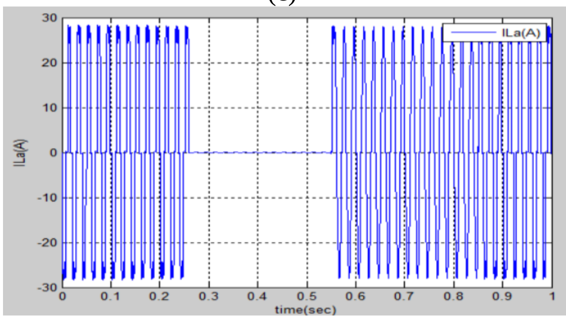

(d)

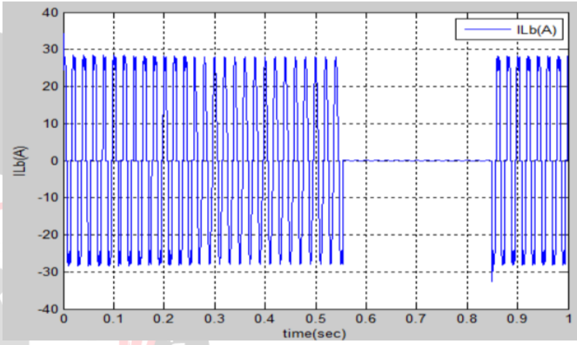

(e)

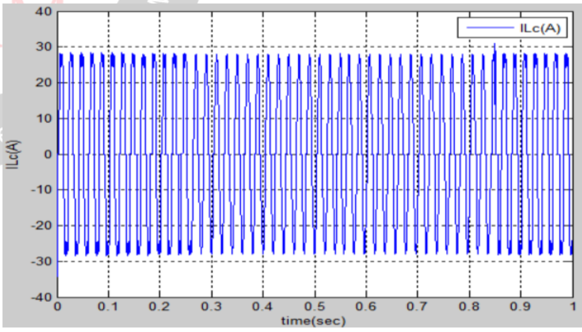

(f)

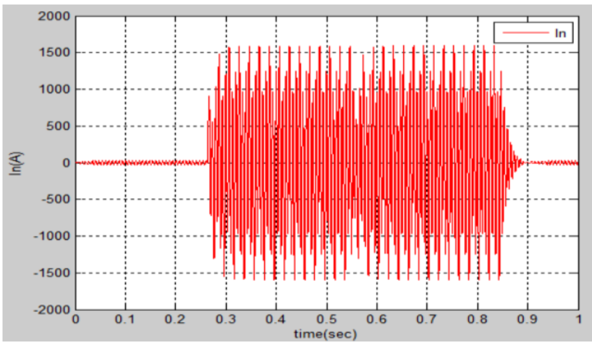

(g)

 DOI : 10.35291/2454-9150.2021.0380

ISSN : 2454-9150 Vol-07, Issue-04, JULY 2021

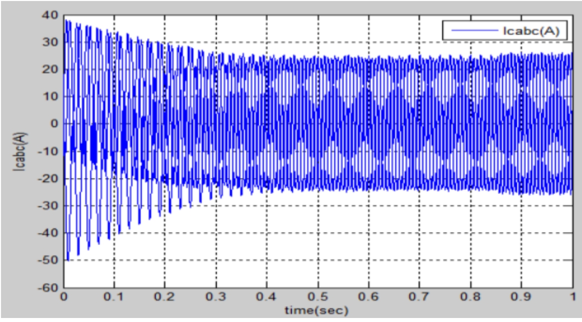

(h)

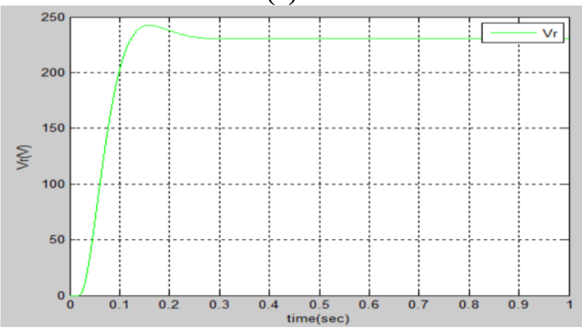

(i)

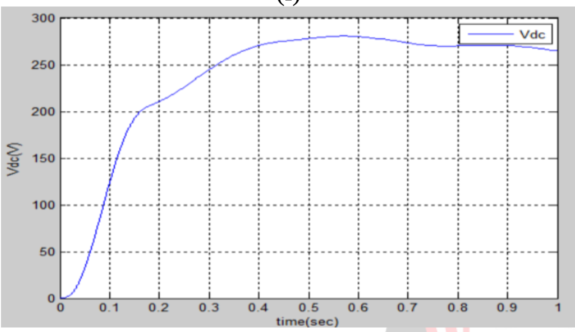

(j)

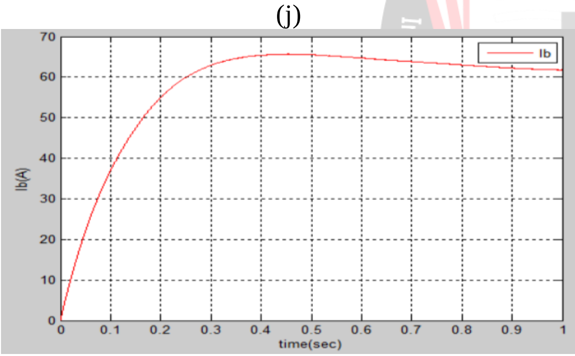

(k)

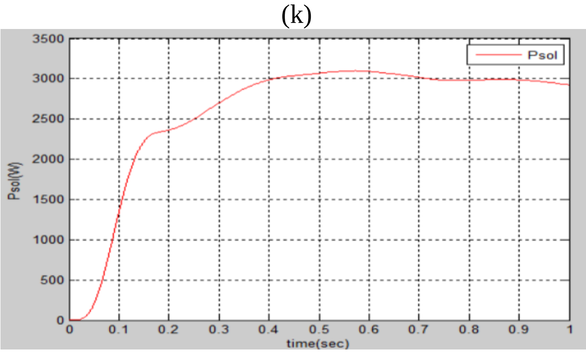

(l)

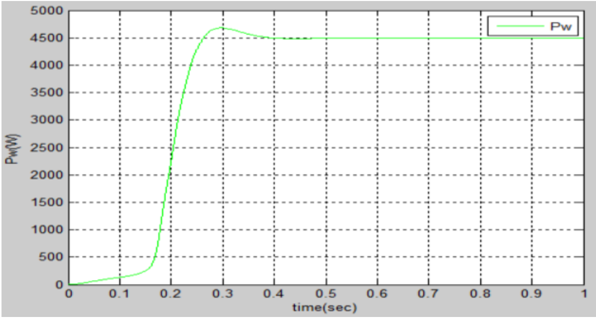

(m)

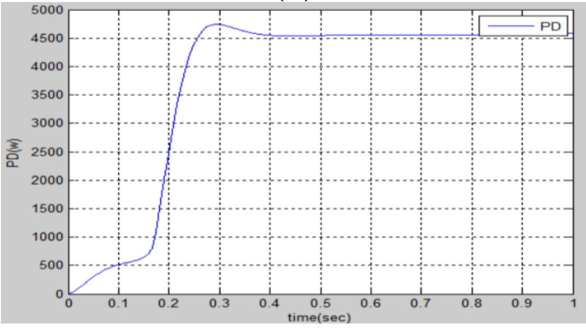

(n)

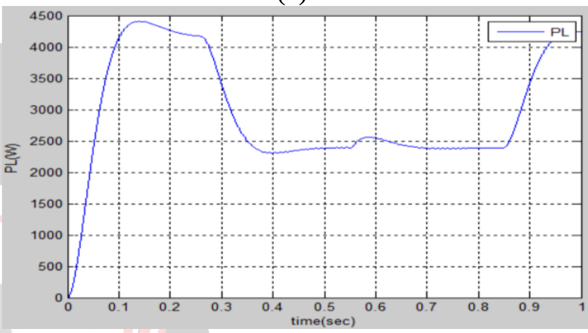

(o)

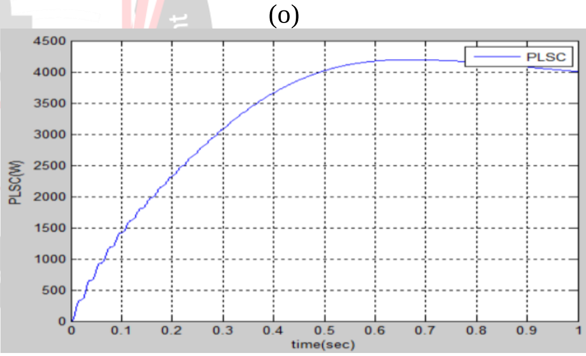

(p)

Fig.13. System performance at nonlinear unbalanced load: V_r, V_{dc}, I_b, P_{sol}, P_w, P_D, P_L and P_{LSC}.

VI. Conclusion

A novel artificial neural network (ANN)-based adaptive PI control doubly fed induction generator (DFIG) driven by a wind turbine has been designed and connected to the DG. PI-ANN algorithm is used to determine the optimal parameters of DFIG PI controllers at different operating points in small signal stability analysis. An ANN which has a simple structure and a sufficient accuracy is designed, trained, and it provides the ability to quickly forecast the optimal parameters. The ANN controllers dynamically change PI gain values according to the different wind speed to increase DFIG transient performance in a global operating range. The simulation results show that the

 DOI : 10.35291/2454-9150.2021.0380

proposed algorithm is highly efficient to reduce DFIG low frequency oscillations. The indices of eigen values, damping ratios, etc, verify that the transient performance of DFIG is significantly improved in a wide wind speed range while the stability is also improved.

REFERENCES

[1] J. Knudsen, J. D. Bendtsen, P. Andersen, K. K. Madsen, and C. H. Sterregaard, "Supervisory control implementation on diesel-driven generator sets," IEEE Trans. Ind. Electron., vol. 65, no. 12, pp. 9698-9705, Dec. 2018.

[2] J. Jo, H. An, and H. Cha, "Stability improvement of current control by voltage feed forward considering a large synchronous inductance of a diesel generator," IEEE Trans. Ind. Applicat., vol. 54, no. 5, pp. 5134-5142, Sept.-Oct. 2018.

[3] Y. Zhang, A. M. Melin, S. M. Djouadi, M. M. Olama and K. Tomsovic, "Provision for guaranteed inertial response in diesel-wind systems via model reference control," IEEE Trans. Power Systems, vol. 33, no. 6, pp. 6557-6568, Nov. 2018.

[4] N. Nguyen-Hong, H. Nguyen-Duc, and Y. Nakanishi, "Optimal sizing of energy storage devices in isolated wind-diesel systems considering load growth uncertainty," IEEE Trans. Ind. Applicat., vol. 54, no. 3, pp. 1983-1991, May-June 2018.

[5] W. Li, P. Chao, X. Liang, J. Ma, D. Xu, and X. Jin, "A practical equivalent method for DFIG wind farms," IEEE Trans. Sustain. Energy, vol. 9, no. 2, pp. 610-620, April 2018.

[6] T. Adefarati, R. C. Bansal, and J. John Justo, "Techno-economic analysis of a PV–wind–battery–diesel standalone power system in a remote area," The Journal of Engineering, vol. 2017, no. 13, pp. 740-744, 2017.

[7] C. Wu and H. Nian, "Stator harmonic currents suppression for DFIG based on feed-forward regulator under distorted grid voltage," IEEE Trans. Power Electron., vol. 33, no. 2, pp. 1211-1224, Feb. 2018.

[8] N. K. Swami Naidu and B. Singh, "Experimental implementation of doubly fed induction generator-based standalone wind energy conversion system," IEEE Trans. Ind. Applicat., vol. 52, no. 4, pp. 3332-3339, July-Aug. 2016.

[9] D. Sun, X. Wang, H. Nian, and Z. Q. Zhu, "A sliding-mode direct power control strategy for DFIG under both balanced and unbalanced grid conditions using extended active power," IEEE Trans. Power Electron., vol. 33, no. 2, pp. 1313-1322, Feb. 2018.

[10] Ju Liu, Wei Yao, Jinyu Wen, Jiakun Fang, Lin Jiang, Haibo He, and Shijie Cheng, "Impact of power grid strength and PLL parameters on stability of grid-connected DFIG wind farm," IEEE Trans. Sustain. Energy, vol. 11, no. 1, pp. 545-557, Jan. 2020.

[11] A. Thakallapelli, S. Kamalasadan, K. M. Muttaqi, and M. T. Hagh, "A synchronization control technique for soft connection of doubly fed induction generator based wind turbines to the power grids," IEEE Trans. Ind. Applicat., vol. 55, no. 5, pp. 5277-5288, Sept.-Oct. 2019.

[12] P. Shah, I. Hussain, and B. Singh, "Single-stage SECS interfaced with grid using ISOGI-FLL-based control algorithm," IEEE Trans. Ind. Applicat., vol. 55, no. 1, pp. 701-711, Jan.-Feb. 2019.

[13] A. K. Singh, I. Hussain, and B. Singh, "Double-stage three-phase grid-integrated solar PV system with fast zero attracting normalized least mean fourth based adaptive control," IEEE Trans. Ind. Electron., vol. 65 no. 5, pp. 3921-3931, May 2018.

[14] M. J. Morshed and A. Fekih, "A novel fault ride through scheme for hybrid wind/PV power generation systems," IEEE Trans. Sustainable Energy, Early Access.

[15] S. K. Tiwari, B. Singh, and P. K. Goel, "Design and control of autonomous wind–solar system with DFIG feeding 3-phase 4-wire loads," IEEE Trans. Ind. Applicat., vol. 54, no. 2, pp. 1119-1127, March-April 2018.

[16] Y. Zhang, J. Wang, A. Berizzi, and X. Cao, "Life cycle planning of battery energy storage system in off-grid wind–solar–diesel micro grid," IET Gener., Trans. & Distr., vol. 12, no. 20, pp. 4451-4461, Nov. 2018.

[17] S. K. Tiwari, B. Singh, and P. K. Goel, "Control of wind–diesel hybrid system with BESS for optimal operation," IEEE Trans. Ind. Applicat., vol. 55, no. 2, pp. 1863-1872, March-April 2019.

[18] K. Venkatraman, B. Dastagiri Reddy, M. P. Selvan, S. Moorthi, N. Kumaresan, and N. A. Gounden, "Online condition monitoring and power management system for standalone micro-grid using FPGAs," IET Gener., Trans. & Distr., vol. 10, no. 15, pp. 3875-3884, Nov. 2016.

[19] S. Puchalapalli and B. Singh, "A single input variable FLC for DFIG-based WPGS in standalone mode," IEEE Trans. Sustainable Energy, vol. 11, no. 2, pp. 595-607, April 2020.

[20] J. Hussain and M. K. Mishra, "Adaptive maximum power point tracking control algorithm for wind energy

 DOI : 10.35291/2454-9150.2021.0380

conversion systems," IEEE Trans. Energy Convers., vol. 31, no. 2, pp. 697-705, June 2016.

[21] S. Puchalapalli, S. K. Tiwari, B. Singh, and P. K. Goel, "A micro grid based on wind driven DFIG, DG and solar PV array for optimal fuel consumption," in 8th IEEE Power India International Conference (PIICON), Kurukshetra, India, 2018, pp. 1-6.

AUTHORS PROFILE

D. Sireesha is an Under Graduate student studying IV B.Tech Electrical and Electronics Engineering from Kallam Haranadhareddy Institute of Engineering & Technology, Guntur, A.P, India. She is one of the toppers in the college who got meritorious scholarship and won many prizes in the technical events held at intra and inter college level. Her research intrests include Power System Operation and Electrical Machines.

Dr. K. Hari Krishna received his B.Tech degree in Electrical & Electronics Engineering from Jawaharlal Nehru Technological University, Kakinada, India in 2003 and M. Tech with Power Systems from Acharya Nagarjuna University, Guntur, India in 2006. He received Ph.D. degree from the Acharya Nagarjuna University, Guntur, India in 2017. He is havng 16 years of teaching and research experience. He is Currently Professor in the Department of Electrical & Electronics Engineering, Kallam Haranadhareddy Institute of Technology, Guntur, India. His Research intrests are in the area of Power System Operation and Stabilty.

 DOI : 10.35291/2454-9150.2021.0380